Faculteit Industriële Ingenieurswetenschappen

master in de industriële wetenschappen: energie

Masterthesis

Optimization of thin film chalcogenide solar cell baseline process

Jelle Van Lommel

Scriptie ingediend tot het behalen van de graad van master in de industriële wetenschappen: energie

PROMOTOR :
Prof. dr. Bart VERMANG

PROMOTOR :
prof. dr. Guy BRAMMERTZ

Gezamenlijke opleiding UHasselt en KU Leuven

UHASSELT KU LEUVEN

Universiteit Hasselt | Campus Diepenbeek | Faculteit Industriële Ingenieurswetenschappen | Agoralaan Gebouw H - Gebouw B | BE 3590 Diepenbeek

Universiteit Hasselt | Campus Diepenbeek | Agoralaan Gebouw D | BE 3590 Diepenbeek
Universiteit Hasselt | Campus Hasselt | Martelarenlaan 42 | BE 3500 Hasselt

UHASSELT KU LEUVEN

2023
2024

Faculteit Industriële Ingenieurswetenschappen

master in de industriële wetenschappen: energie

Masterthesis

Optimization of thin film chalcogenide solar cell baseline process

Jelle Van Lommel

Scriptie ingediend tot het behalen van de graad van master in de industriële wetenschappen: energie

PROMOTOR :
Prof. dr. Bart VERMANG

PROMOTOR :
prof. dr. Guy BRAMMERTZ

UHASSELT KU LEUVEN

PREFACE

I am immensely grateful to those who have supported me throughout my academic journey and the completion of this Master's thesis. First and foremost, I would like to express my deepest gratitude to my family for their unwavering love, encouragement, and understanding. Their constant support has been my anchor, guiding me through both the challenges and successes of this endeavor.

I extend my heartfelt appreciation to my supervisors, Prof. dr. Guy Brammertz and Prof. dr. Bart Vermang, for their invaluable guidance, expertise, and encouragement throughout this research. Their insightful feedback, patience, and mentorship have been instrumental in shaping the direction of this thesis and in my personal and academic growth.

The inspiration why I chose this subject stems from my profound interest in renewable energy and its potential to transform our world. I chose this subject because I am passionate about exploring innovative solutions to address the pressing challenges of climate change and sustainability. Renewable energy, with its promise of clean, sustainable power, has always captivated my imagination, and I am honored to contribute to the field through this research.

This thesis represents the culmination of months of dedication, hard work, and perseverance. It is my hope that the findings presented here will contribute to the existing body of knowledge in the field of renewable energy and inspire further research and innovation.

Once again, I extend my deepest gratitude to my family, supervisors, and all those who have supported me on this journey. This achievement would not have been possible without your support, guidance and encouragement.

CONTENTS

Preface **1**

List of tables **6**

List of figures **8**

List of acronyms and abbreviations **10**

Abstract **13**

Abstract in Dutch **15**

1 Introduction **17**
1.1 Context . . . 17
1.2 Problem statement . . . 17
1.3 Objectives . . . 18
1.4 Materials and methods . . . 18

2 Literature study **19**
2.1 Structure of CIGS cells . . . 19
2.1.1 Glass substrate . . . 19
2.1.2 Molybdenum back contact . . . 19
2.1.3 Absorber layer . . . 19
2.1.4 Buffer layer . . . 20
2.1.5 Window layer . . . 20
2.2 Deposition methods for the absorber layer . . . 20
2.2.1 Vacuum processes . . . 21
2.2.2 Non-vacuum processes . . . 22
2.2.3 comparison of absorber fabrication processes . . . 23

3 Experiments **25**
3.1 One factor at a time experiment . . . 25
3.1.1 Absorber layer fabrication . . . 25
3.1.2 Absorber layer characterization . . . 27
3.1.3 solar cell characterization . . . 27
3.1.4 Statistical analysis software . . . 27
3.1.5 Results and discussion . . . 28
3.2 Baseline stability experiment . . . 30
3.2.1 Results and discussion . . . 31
3.3 Finding a new baseline . . . 31
3.3.1 Results and discussion . . . 32
3.4 Anti reflection coating . . . 34
3.4.1 Results and discussion . . . 34

4 Conclusion and outlook **36**

References **39**

A Appendix **40**

B Appendix **41**

LIST OF TABLES

2.1 Differences between RTP and Normal Annealing of CIGS 22
2.2 List of various growth methods used for the preparation of CIGS films, and their advantages and disadvantages 24

3.1 OFAT parameters 27
3.2 Conclusions of important parameters from OFAT versus the old baseline 31
3.3 new baseline versus old baseline 32
3.4 Comparison of the champion cell versus the world record 34

4.1 FFD parameters 36

LIST OF FIGURES

1.1 Big graphite box . . . 17
1.2 Annealsys AS-One furnace . . . 18
1.3 Measuring devices for CIGS absorber layer . . . 18

2.1 Representation of the standard stack of a CIGS-based solar cell . . . 19
2.2 schematic representation of the different deposition methods . . . 20
2.3 Configuration for multi-source elemental co-evaporation reactor . . . 21
2.4 3-stage co-evaporation process . . . 22

3.1 representation of structure of the metal precursor . . . 25
3.2 Annealsys AS-one chamber view . . . 25
3.3 Sample PV23-14-1 :Baseline Temperature-Sccm-time graph . . . 26
3.4 Boxplots of the efficiency of the OFAT experiment . . . 28
3.5 Influence of Post anneal time (X8) and pump out temperature (X9) on the FF . . . 29
3.6 Influence of Ramping speed (X3), anneal temperature (X4), anneal time (X6), sulphurisation time (X8) and pump out temperature (X9) on the V_{oc} . . . 29
3.7 Old versus new graphite box . . . 30
3.8 Graphite box after ZnO depositioning . . . 30
3.9 Efficiency comparison between new box and old ZnO deposited box . . . 31
3.10 comparing the old with the new baseline . . . 33

A.1 Best solar cell efficiencies . . . 40

B.1 small graphite box 3D design . . . 41
B.2 lid for small graphite box 3D design . . . 42

AAS Atomic Absoption Spectroscopy. 21

Ag Silver. 34–36

ARC anti-reflective coating. 34

a-Si, TF-Si amorphous thin-film silicon. 17

CdS cadmium sulfide. 20, 34

CdTe cadmium telluride. 17

CGS Copper Gallium Selenium. 24

CIGS Copper indium gallium disulfide diselenide $Cu(In, Ga)(S, Se)_2$. 6, 8, 13, 15, 17–20, 22–24, 34–36

CIS Copper Indium Selenium. 24

Cu copper. 20–23, 25, 27

E_g bandgap energy. 34, 35

EDS Energy-dispersive X-ray Spectroscopy. 27

FF fill factor. 8, 27, 29, 32–35

FFD Full Factorial Design. 18, 31, 36

Ga gallium. 20–25, 27, 34

green 532nm laser diode pumped solid state laser. 27

H_2 hydrogen. 26

H_2S hydrogen sulfide. 22, 26, 36

H_2Se hydrogen sulenide. 22, 24, 26

In indium. 20–23, 25, 27

ITO Indium doped Tin Oxide. 20, 34

J_{sc} short circuit density. 27, 32–35

MgF_2 magnesium fluoride. 34

Mo Molybdenum. 19, 21, 25, 34

$MoSe_2$ Molybdenum diselenide. 19

N_2 nitrogen. 22, 26

OFAT One Factor A Time. 6, 8, 13, 15, 18, 25–28, 30–32, 36

PDT Post-deposition treatment. 34–36

PL photo-luminescence spectroscopy. 13, 15, 18, 27

R_s series resistance. 27, 32, 33

R_{sh} shunt resistance. 27, 32, 33

RbF Rubidium fluoride. 34, 36

RTP Rapid Thermal Processing. 22, 25

S Sulphur. 22

sccm Standard Cubic centimeter per minute (cm^3/min). 26, 27, 32

Se Selenium. 21–23, 25, 27

SEM Scanning Electron microscopy. 13, 15, 18, 27

SLG Soda Lime Glass. 19, 21, 25

V_{oc} open-circuit voltage. 8, 27, 29, 32–35

ZnO Zink oxide. 8, 20, 30, 31

ABSTRACT

At Energyville in Genk, the imo-imomec group conducts research into thin-film CIGS solar cells. The absorber layer of CIGS solar cells is produced with the two-step process in Energyville and has two main working points. On the one hand, the conversion efficiency of the baseline champion cells is 12%, which is significantly lower than the conversion efficiency world record of 23.6%. On the other hand, the stability of these champion cells is not always the same. This master's thesis aimed to solve the stability problem and also to improve efficiency by 2-3%.

To gain a better understanding of the correlation between absorber properties and measured cell efficiencies, the current baseline was analyzed. After this, an OFAT experiment was conducted and the samples were characterized with SEM, PL and I-V measurements. Finally, statistical analysis software was used to find a model out of the OFAT. This knowledge was then tested into a new baseline recipe. To solve the stability problem, a new graphite box was designed and ordered.

The newly designed graphite box solved the stability problem because it contains less graphite and is saturated during the selenization. The statistical analysis software showed the importance of five of the nine parameters, but due to the stability problem at the time of the OFAT experiment, it was not able to make a perfect model out of it. Nevertheless, the baseline recipe was adjusted with this knowledge and this resulted in champion cell efficiency of 16.7%.

ABSTRACT IN DUTCH

Bij Energyville in Genk, doet de imo-immomec groep onderzoek naar dunne film CIGS zonnecellen. De absorptie laag van de CIGS zonnecellen in Energyville wordt er geproduceerd met het twee-staps proces en heeft twee grote werkpunten. Enerzijds is de efficiëntie van de beste cellen 12% en dat is significant lager dan de 23.6% van het wereldrecord. Anderzijds is de stabiliteit van de geproduceerde cellen niet altijd dezelfde. Deze masterproef heeft als doel om het stabiliteitsprobleem op te lossen en ook om de efficiëntie te verbeteren met 2-3%.

Om een beter begrip te krijgen van de verbanden tussen de absorber eigenschappen en de gemeten cel efficiëntie zal eerst het huidige recept worden geanalyseerd. Hierna vind er een OFAT-experiment plaats waarvan de staaltjes worden gekarakteriseerd met de SEM, PL alsook met I-V metingen. Ten slotte wordt statistische analysesoftware gebruikt om een model uit de data te vinden. Deze ken- nis wordt dan gebruikt om een nieuw recept te ontwikkelen. Om het stabiliteitsprobleem op te lossen is een nieuwe grafietdoos ontworpen en besteld.

De nieuwe grafietdoos, was kleiner en bevatte minder grafiet waardoor deze wel verzadigd raakte bij selenizatie. De analysesoftware toonde het belang van vijf van de negen parameters aan, maar was vanwege het stabiliteitsprobleem ten tijde van het OFAT-experiment niet in staat er een perfect model van te maken. Toch werd met deze kennis het basisrecept aangepast en dit resulteerde in een efficiëntie van 16.7% voor de kampioenschaps cellen.

1.1 Context

In a world where it is necessary to phase out fossil energy due to its effect on global warming. Solar energy is a good alternative to fossil energy. The most well-known way of harvesting solar energy is with silicon-based solar cells, but silicon-based solar cells have some physical limits and are therefore not applicable everywhere. In addition to silicon-based solar cells, thin-film solar cells are able to fill that gap. They can be used in different applications that require them to be lightweight or flexible. There are different types of thin film solar cells such as cadmium telluride (CdTe), amorphous thin-film silicon (a-Si, TF-Si), or Copper indium gallium disulfide diselenide $Cu(In, Ga)(S, Se)_2$ (CIGS). In the imo-imomec group of Imec and the University of Hasselt, the research focuses on the optimization of CIGS solar cells. All of this research occurs within the laboratories of the Energyville 2 campus in Genk. The CIGS samples in the Energyville 2 laboratories have the following structure: the substrate, back contact, absorber layer, buffer layer, and finally the window layer (see figure 2.1 [1]).

This master's thesis focuses on the optimization of the absorber layer. To form this layer, the imo-imomec group uses a two-step process. The first step in this process is the deposition of the metals (Cu, In, Ga) using a standard, low-cost, and low-temperature method that delivers a uniform composition. The second step is the annealing of the sample in a Selenium (Se) atmosphere.[2] This is also known as the selenization of metal precursors.

1.2 Problem statement

The problem of the CIGS solar cells that are created at the imo-imomec group is that the power conversion efficiency of the champion cells is 12% and is lower than the world record efficiency of 23. 6% measured in Uppsala University (see Appendix A) . Furthermore, there is the problem that the existing baseline is not stable and produces other efficiencies on different runs with the same recipe. Therefore, it is important to better understand the important parameters in the two-step process, because during selenization the samples are placed in a graphite box (see figure 1.1) and this box consumes Se, S, and other elements that transform into the gas phase. This causes a serious memory effect in the box, where it releases different amounts of the consumed elements during different runs.

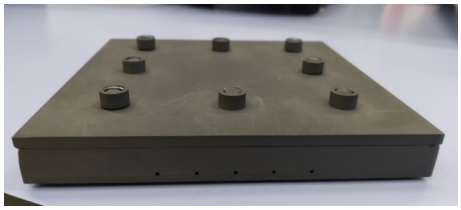

Figure 1.1: Big graphite box

1.3 Objectives

The main objective is that by the end of this master's thesis, the power conversion efficiency of the CIGS solar cells made in the imo-imomec group is 2-3% higher than the current efficiency and also stable. To achieve this first, it is important to gain a better understanding of the parameters that affect the two-step process. What parameters have a good, bad, or no influence on efficiency. Secondly, Providing a solution for the memory effect issues.

1.4 Materials and methods

The first task will involve the statistical analysis of the current baseline. Insight into the correlation between absorber properties and measured cell efficiencies might lead to a better understanding of the limitations of the technology. Subsequently, training was provided on the absorber fabrication selenization process in the annealing furnace (see Figure 1.2) and on the main characterization techniques to determine the quality of the material and the electrical properties. These techniques are Scanning Electron microscopy (SEM) [3], photo-luminescence spectroscopy (PL) and current-voltage measurements (IV measurements) (see Figure 1.3). These tools will be further explained in the following sections 3.1.2.1,3.1.2.2 and 3.1.3

Figure 1.2: Annealsys AS-One furnace used for selenization of CIGS samples[4]

After training on the tools is performed, solar cells are manufactured using different optimization approaches. At the start of this master's thesis the approach of a Full Factorial Design (FFD) experiment is not possible. This is due to the fact that a FFD experiment necessitates the exploration of all conceivable parameter combinations, which, in our specific context, would result in an impractically large number of permutations. Therefore, a One Factor A Time (OFAT) experiment was chosen. These solar cells will be measured with the techniques described above, and the electrical measurement results will be correlated with the properties of the measured material.

(a) Oriel IV setup

(b) SEM [5]

(c) PL

Figure 1.3: Measuring devices for CIGS absorber layer

2.1 Structure of CIGS cells

A CIGS solar cell comprises a sequence of four distinct thin films, each composed of materials, layered on a substrate [1],[6]. In this order, you can find the layers on top of the substrate: the back contact, the absorber layer, the buffer layer, and the window layer (see Figure 2.1) [1].

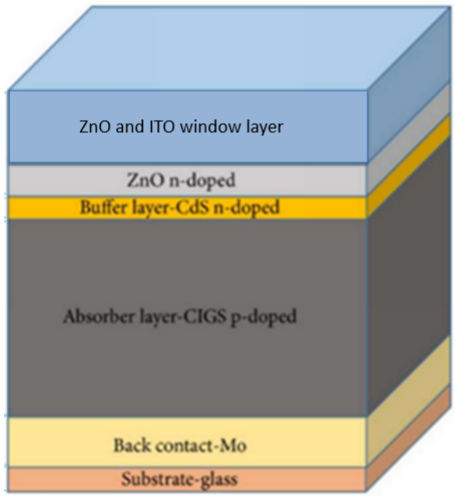

Figure 2.1: Representation of the standard stack of a CIGS-based solar cell [1, p.2]

2.1.1 Glass substrate

The substrate is the base layer upon which the solar cell is built. In a laboratory environment, the substrate is generally Soda Lime Glass (SLG). This is primarily because SLG is an insulator and has a thermal coefficient that is more or less the same as the absorber layer (see 2.1.3) and therefore there will be fewer thermal stresses during the production process of the different layers [1],[6].

2.1.2 Molybdenum back contact

On the SLG a Molybdenum (Mo) film of $\pm 0.5\mu$m is sputtered that will serve as the back electrode[2]. The function of the back electrode is to gather all the energy carriers, and Mo is suited for this because between the absorber layer and Mo an interfacial layer of Molybdenum diselenide ($MoSe_2$) is formed. This $MoSe_2$ gives a good ohmic contact and is therefore a good back electrode. Another benefit of utilizing Mo as your back contact is that it allows sodium from SLG to migrate through the Mo layer to the absorber layer[1][2],[7].

2.1.3 Absorber layer

The core component of the solar cell is the absorber layer [8] and it is responsible for the conversion of sunlight into electrical energy. [9] When sunlight strikes the absorber layer, the semiconductor materials absorb photons of light energy. This absorption process creates electron-hole pairs within

the material, where electrons are excited to a higher-energy state, leaving behind positively charged holes.The electron-hole pairs undergo charge separation because of the built-in electric field within the absorber layer. Electrons migrate toward the front contact, while holes move toward the back contact, creating a potential difference or voltage across the solar cell. This flow of charge carriers constitutes an electrical current. The absorber layer is made up of Copper indium gallium disulfide diselenide $Cu(In, Ga)(S, Se)_2$ (CIGS). Where copper is the primary conductive material in the absorber layer, the ratio indium and gallium is essential to adjust the band gap over a wide range, allowing maximizing the absorption of sunlight for maximum efficiency.

2.1.4 Buffer layer

Directly on top of the absorber layer is the buffer layer, usually made of a compound such as cadmium sulfide (CdS). The buffer layer helps to improve the efficiency of the cell by facilitating the flow of electrons from the absorber layer to the front contact. It is negative-doped (n-type), and in combination with the p-type absorber layer it forms the PN-Junction of the solar cell. CdS also passivates the surface defects of the absorber layer.

2.1.5 Window layer

The window layer is transparent and is made up of Zink oxide (ZnO) and Indium doped Tin Oxide (ITO) which form two inner layers in the window layer. The ZnO inner layer is $\pm$50 nm thick and is a N-type semiconductor that will limit electronic losses. The other inner layer ITO is 150 nm thick and is the front electrode that collects all energy carriers [1].

2.2 Deposition methods for the absorber layer

The development of CIGS absorber layers occurs in a temperature range of 450 to 600°C to produce a superior quality product. Despite the existence of numerous deposition techniques, only a handful are prevalent in both small-scale laboratory and large-scale industrial manufacturing [10]. These dominant deposition techniques (see Figure 2.2) can be broadly divided into vacuum and non-vacuum processes [10],[11]. These two categories will be described in the following subsections 2.2.1, 2.2.2 and will be compared in 2.2.3.

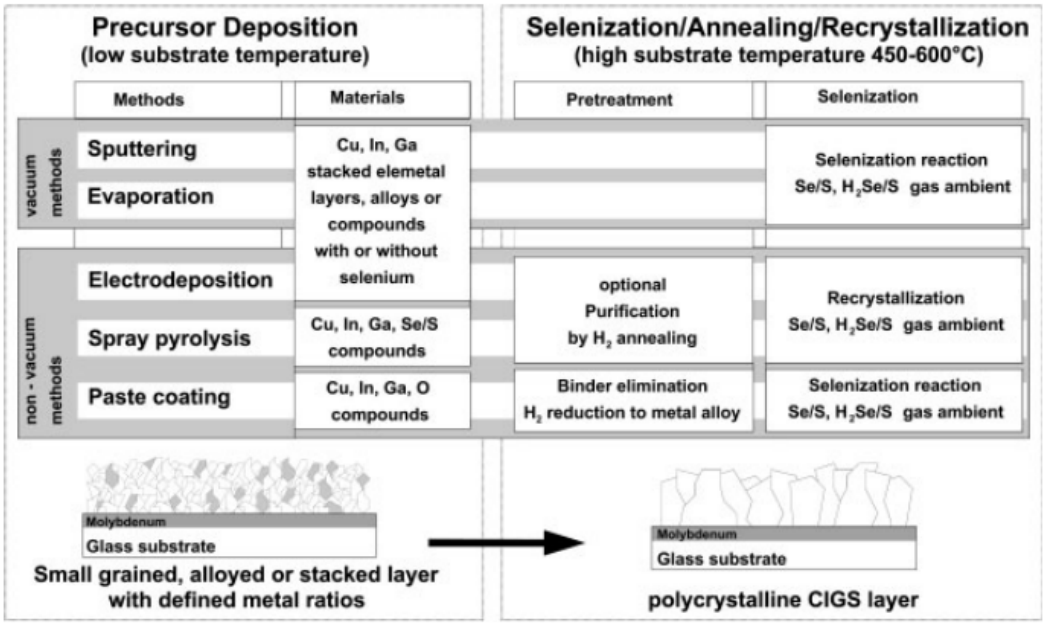

Figure 2.2: schematic representation of the different deposition methods [11, p. 100]

2.2.1 Vacuum processes

Vacuum processes can be divided into two different techniques, namely co-evaporation (2.2.1.1) and two-step processes (2.2.1.2). These two techniques are the most dominant for producing the absorber layer because they produce the highest efficiencies [12].

2.2.1.1 Co-evaporation process

With the co-evaporation method the Mo-coated SLG-substrate is placed in a vacuum chamber (see Figure 2.3) together with the source elements, namely Cu, In, Ga and Se. These elements are heated beyond their evaporation points to produce vapor-phase atoms [13]. "While the evaporation temperatures for each metal will depend on the specific source design, typical ranges are 1300 to 1400°C for Cu, 1000 to 1100°C for In, 1150 to 1250°C for Ga, and 300 to 350°C for Se evaporation" [2, p. 580]. These vapor atoms condense against the SLG-substrate and form the absorber layer. The growth monitor uses Atomic Absoption Spectroscopy (AAS)[1] to control the elemental flux and the composition of the CIGS film is monitored using X-ray fluorescence [10].

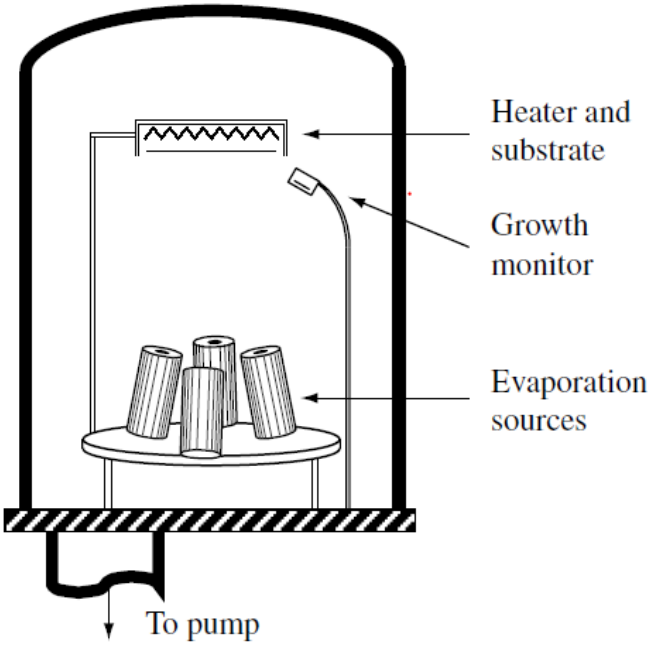

Figure 2.3: Configuration for multi-source elemental co-evaporation reactor [2, p. 580]

There are several types of co-evaporation processes, but the most used is the 3-stage co-evaporation process (see Figure 2.4), because this process has the in-line compatibility for the mass production of high-performance modules [10]. During all 3 stages of the process, a steady Se flux is maintained [7]. In the first stage In and Ga were evaporated, followed by the evaporation of Cu in the second stage until the film reaches the desired composition, and finally in the third stage In and Ga are again evaporated until $Cu(InGa)Se_2$ is reached [2][13][14].

[1] Atomic Absoption Spectroscopy (AAS)is a technique used in analytical chemistry to determine the concentration of specific metal elements in a sample. AAS is used as a growth monitor during the co-evaporation process. This process involves heating elements to their evaporation points in a vacuum chamber, where they vaporize and then condense on a substrate to form an absorber layer. Using AAS, the composition and thickness of the absorber layer can be precisely monitored, ensuring the quality and consistency of the material being produced.

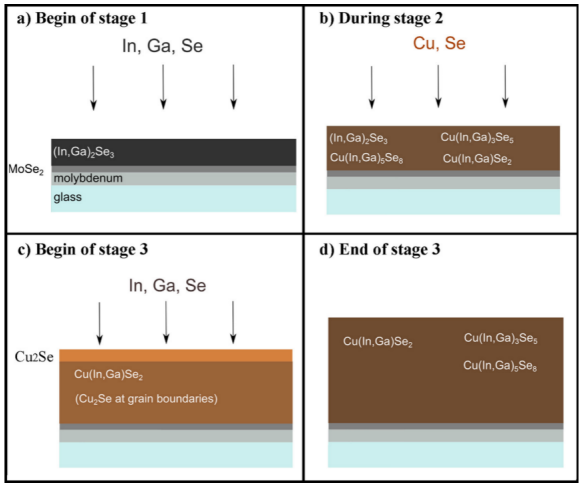

(a) Different stages [13, p. 2]

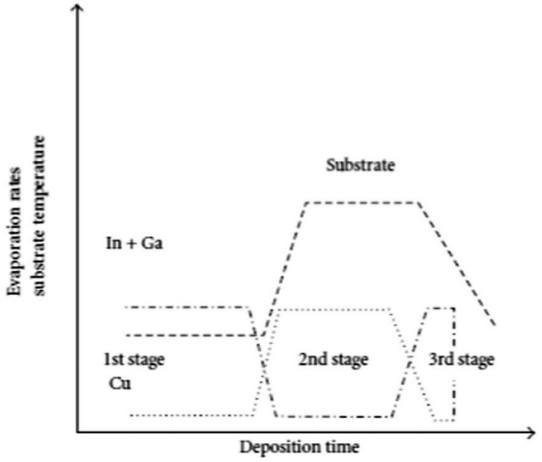

(b) substrate deposition rates and temperature [10, p. 1312]

Figure 2.4: 3-stage co-evaporation process

2.2.1.2 Two-step process

The second vacuum technique is named the two-step process. It is a two-stage deposition process in which Cu, In and Ga elements are sputtered onto the substrate and then annealed in a Sulphur / Selenium containing atmosphere for the formation of a CIGS film [15].Sputtering is a favored technique for the first step because of its scalability with commercially available deposition tools, ensuring consistent coverage across extensive surfaces at rapid deposition speeds [2]. In the second step, the precursor film is commonly annealed in a furnace (e.g. tube furnace) with H_2Se,H_2S, Se or S vapor at temperatures ranging from 400 to 600°C for 30 to 60 minutes to produce optimal device quality material [2],[10]. Although these hydride gases are poisonous, their high reactivity and ease of control present benefits. The employment of Rapid Thermal Processing (RTP) can circumvent the issue of toxic gases [10]. With RTP the metallic precursor does not only contain Cu,In and Ga, but also Se before it is placed in a RTP furnace (shown in Figure 1.2). To prevent the formation of toxic compounds, these RTP furnaces operate in an inert gas atmosphere. This inert gas is typically N_2 or a combination of N_2 and H_2S. Table 2.1 summarizes the differences between a normal annealing process and Rapid Thermal Processing (RTP). The Rapid Thermal Processing is used during all the experiments of this master's thesis, and a step-by-step explanation of the process can be found in subsection 3.1.1.

Table 2.1: Differences between RTP and Normal Annealing of CIGS

Rapid Thermal Processing	Normal Annealing Process
Fast heating rates	Slow heating rates
Short processing times	Longer processing times
Minimizes thermal budget	Higher thermal budget
Smaller grains	larger grains
More effective for activating dopants	Less effective for activating dopants
special designed RTP furnace	various types of furnace can be used

2.2.2 Non-vacuum processes

Elevated production expenses and intricate vacuum procedures have prompted the creation of straightforward and economical non-vacuum methods [10], [16]. These processes can best be compared to the two-step vacuum process, because there will also be a precursor deposition at low temperatures followed by a selenization at high temperatures. The different non-vaccuum processes studied for this master's thesis are paste coating, spray pyrolysis, and electrodeposition [10].

2.2.2.1 Paste coating process

For paste coating, first, a paste containing the precursor materials (Cu,In,Ga,Se) along with binders and solvents is mixed to make a homogeneous paste. Next, this paste is coated onto the substrate using various coating techniques, such as screen printing, doctor blade coating, or spray coating [10]. When the paste is depositioned, the coated substrate is dried to remove the solvent from the paste. This drying step can be performed using air drying or infrared heating. Finally, the dry paste-coated substrate is subjected to thermal treatment to convert the precursor materials into the final CIGS absorber layer [17][18].

2.2.2.2 Spray pyrolysis process

In spray pyrolysis processes, salts are disolved with Cu,In,Ga and Se compounds into a suitable solvent. This solution is atomized into fine droplets and sprayed onto the substrate surface. The spray nozzle is moved across the substrate to ensure uniform coverage and thickness of the deposited layer. As the droplets land on the heated substrate (200-300°C), the solvent in the sprayed solution evaporates rapidly as a result of the high substrate temperature, leaving behind a thin film of precursor material. Finally a pyrolysis thermal treatment happens and the CIGS absorber layer is formed [19].

2.2.2.3 Electrodeposition process

The electrodeposition process starts with the preparation of an electrolyte solution were Cu,In,Ga and Se are dissolved in a suitable electrolyte solution. In addition, stabilizers and additives are added to control the deposition parameters. A substrate is then immersed in the electrolyte solution, serving as the cathode, while a counter electrode (anode) is also placed in the solution. When a voltage is applied across the electrodes, the precursor ions in the solution are reduced at the cathode (substrate surface), leading to the deposition of the CIGS layer. After electrodeposition, the substrate was rinsed to remove any residual electrolyte solution and prevent contamination. In the final step, the electrodeposited precursor layer is subjected to thermal treatment to convert it into the final CIGS absorber layer [10],[20].

2.2.3 comparison of absorber fabrication processes

In this section, the advantages and disadvantages of all different absorber fabrication processes are compared. Upon examining vacuum and non-vacuum processes in general, the non-vacuum processes have lower equipment costs, a simpler setup, and are easier to scalable. However, vacuum processes have better control over the film quality, and the most important is that they still result in higher efficiencies than non-vacuum processes. Therefore, vacuum is still used more, but the potential of non-vacuum can not be denied. A more detailed overview of the different techniques can be found in Table 2.2.

Table 2.2: List of various growth methods used for the preparation of CIGS films, and their advantages and disadvantages [10, p.1313]

Methods	Advantages	Disadvantages
Co-evaporation	Well established technique for lab-scale devices	Simultaneous control of sources is difficult and results in variation in stoichiometry, poor reproducibility and uniformity over large area
Sputtering	Controlled deposition rate and better crystallinity	High operational cost, produces multiple phases, CIS, CGS
Selenization/sulfurization	Large area deposition, established technique can be used for precursor deposition and reaction	Toxic gases (H_2Se), additional processing step is required, poor adhesion with back contact
Screen printing	Little material wastage, high packing density, high throughput	Control of Ga profile is not possible, while drying, phase segregation and inhomogeneities occurs
Spray coating	Scalable, high throughput and low cost	Precursor material wastage during spray coating
Doctor blade	Less material wastage, roll-to-roll compatible, better stoichiometric control	Solvent evaporation is slow which leads to accumulation

3.1 One factor at a time experiment

3.1.1 Absorber layer fabrication

For the design of this experiment, a One Factor A Time (OFAT) experiment is chosen. This implies that for each sample, a single parameter is systematically changed to ascertain its influence on the absorber layer. For the fabrication of the absorber layer, the two-step process is used. Upon the Molybdenum Soda Lime Glass the copper and gallium are sputtered together at a temperature of 30 ° C, then the indium layer is sputtered at 150 ° C. This procedure is repeated ten times to achieve a stack of 10 layers as shown in Figure 3.1. On top of this stack a 2-3µm layer of Selenium is capped [21].

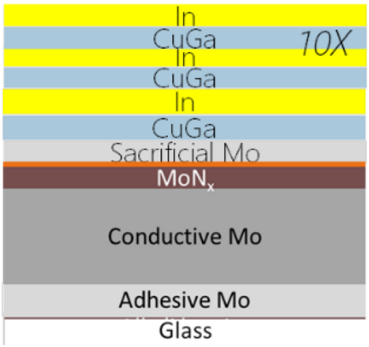

Figure 3.1: representation of structure of the metal precursor

The metallic precursor is then placed in a graphite box as shown in Figure 1.1 before being placed in the Annealsys-AS one Rapid Thermal Processing (RTP) system [22] (see Figure 1.2) for the selenization step. The graphite box will ensure that on 5cm x 5cm samples, the gases and heat are distributed at an even pace. Then it is placed in the chamber as shown in Figure 3.2.

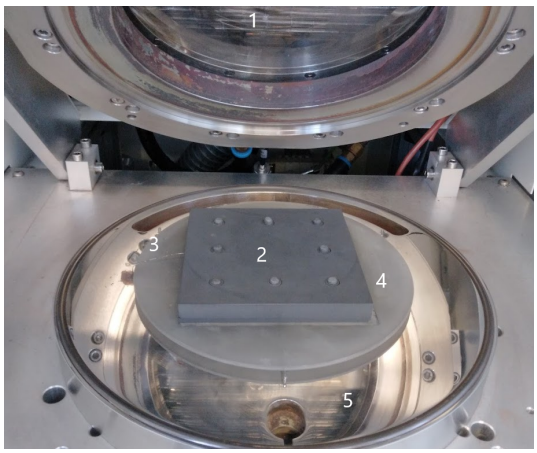

Figure 3.2: chamber view of a annealsys AS-one with 1) Lamp furnace, 2) graphite box, 3) thermocouple, 4) quartz plate, 5) bed plate

The chamber is fitted with a venting purge gas line and four distinct process gas lines, each controlled by mass flow controllers [6]. Gases such as nitrogen (N_2),hydrogen (H_2), hydrogen sulfide (H_2S), and 10% hydrogen sulenide (H_2Se) in N_2 dilution may be injected into the chamber, with upper limits on flow rates of 2000 sccm for N_2 and H_2, and 1000 sccm for H_2S and H_2Se. Users can manipulate various process parameters using the Annealsoft software to control the recipe, this is where the OFAT starts with the baseline recipe [6].

The different baseline selenization steps are shown in Figure 3.3 and operate as follows:

- Venting and pumping (T0): Initiated at the start of the annealing process, this step involves purging the chamber twice using N_2 and once using H_2S to remove any gases and particles, thereby preventing contamination during the subsequent selenization step. Throughout this phase, the chamber maintains room temperature and is subjected to vacuum conditions to prepare for the following ramping stage [6].
- Ramping (T1): In this phase, the temperature within the reaction chamber is gradually increased to the target annealing temperature of 570°C at a consistent rate. The lamp power is adjusted during this process to maintain a temperature increase of 10°C/s. At the same time, H_2S is fed into the reaction chamber at a steady rate of 20 sccm for the baseline to prevent excessive pressure buildup.
- Main anneal (T1 + T2): Upon reaching the annealing temperature, the annealing process starts [6]. The H_2S is still flowing but it will cease after 5 minutes followed by 5 minutes without H_2S flow, but still with the same annealing temperature.
- Post anneal (T3): can also be called the second annealing step. While the temperature is still the same as during the main anneal, there will be a short burst of H_2S with a pressure of 20mbar followed by 1 minute without H_2S flow.
- Cooling process: After the post anneal furnace lamps are turned off, and a waiting period ensues until the graphite box reaches a temperature of 400°C. Upon reaching 400°C, a routine post-process begins to purge the reactor. At this stage, the reactor undergoes an additional venting and pumping cycle to eliminate any remaining gases. [6]. Finally, the sample is removed from the reactor, marking the completion of the selenization process [6].

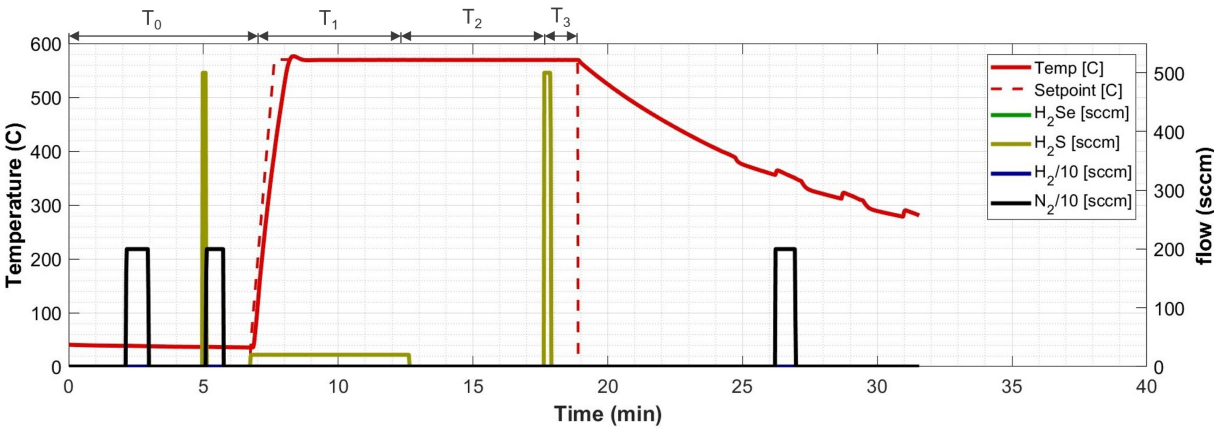

Figure 3.3: Sample PV23-14-1 :Baseline Temperature-Sccm-time graph

In Table 3.1 all parameters of the OFAT experiment are shown. there are 9 parameters, this together with 4 baseline runs ensures that the experiment consists of 22 samples.The baseline parameters are chosen on the basis of existing know-how within the group. The outer boundary parameters (- and +) are chosen from a variety of reasons, such as staying under atmospheric pressure to make sure that no gasses escape or hardware limits because the ramp rate could not exceed 15 C/s.

Table 3.1: OFAT parameters

Parameter number	Parameters	Unit	-	Baseline	+
X1	H_2S pressure T_0	mbar	0	30	150
X2	N_2 pressure T_0	mbar	0	670	300
X3	Ramping speed	C/s	2	10	15
X4	Anneal temperature	C	550	570	590
X5	H_2S flow during T_1	sccm	0	20	40
X6	Anneal time T_1 + T_2	min	2+2	5+5	10+10
X7	H_2S pressure post-anneal	mbar	0	20	100
X8	Post-anneal time T_3	min	0	1	3
X9	Pump out temperature	C	100	400	550

3.1.2 Absorber layer characterization

Immediately after the absorber layer is finished in the Annealsys-AS One furnace, the sample must be characterized with photo-luminescence spectroscopy (PL) and Scanning Electron microscopy (SEM). This must be done before the top layers are added.

3.1.2.1 Photoluminescense microscopy

The Fluotime300 fluorescence spectrometer (see Figure 1.3c), manufactured by PicoQuant and equipped with a diode pumped solid state laser (green 532nm laser), that will be used to determine the bandgap of the heat treated absorber material. Measurement of this bandgap provides insight into the integration of gallium within the CIGS structure of the selenized samples. Additionally, the spectrometer is used to perform lifetime measurements, offering further details on the absorber layer's quality. Multiple tests were performed in various sections of the sample to assess its uniformity [6].

3.1.2.2 Scanning electron microscopy

The Vega3 SEM from Tescan (see Figure 1.3b) assesses the structure of the absorber layer and assists in the analysis based on imaging of various samples. Concurrently, Energy-dispersive X-ray Spectroscopy (EDS) measurements are performed with the scanning electron microscope to quantitatively determine the concentrations of Cu, In, Ga, and Se at specific locations on the samples. Micrographs of all samples will be taken using an acceleration voltage of 15 kV, magnifications of 1x to 20kx, and the intensity of the beam changing from 7 to 12 [6].

3.1.3 solar cell characterization

Assessing solar cell performance requires current-voltage measurements. "The electrical parameters, conversion efficiency, open-circuit voltage (V_{oc}), short circuit density (J_{sc}),fill factor (FF), series resistance (R_s) and shunt resistance (R_{sh}) can be extracted from measured illuminated and dark J-V curves" [6, p.27]. These evaluations will be conducted using the oriel solar simulator after the samples have been developed into complete solar cells. The procedure involves the use of two probes, one linked to the back contact and one to the center of the solar cell. Data is captured on a computer via the source meter. The solar cell is tested under dark conditions and under illuminated conditions. The measured electrical behavior of cells is defined by the parameters mentioned above [6].

3.1.4 Statistical analysis software

All of the OFAT data obtained from current-voltage measurements (3.1.3), SEM (3.1.2.2) and PL (3.1.2.1) are entered into a statistical analysis software named JMP. This software will look for connections between the different parameters of the OFAT experiment to form a model out of it.

3.1.5 Results and discussion

In this subsection, the efficiency results of the OFAT experiment are examined. Furthermore, we will also discuss which parameters are considered important and less important on the basis of the JMP software. The efficiency results can be found in Figure 3.4 and the important parameters in Figures 3.5 and 3.6. The first observation that follows from the experiment is that the baseline recipe is not stable (see Figure 3.4) They have an average efficiency between 8% and 11%. A possible explanation for this is that the graphite box is too big and contains too much graphite. Therefore, the graphite of the box will absorb and release different amounts of gasses during different recipes because it is not saturated. The solution for this problem is discussed in a next experiment in section 3.2.

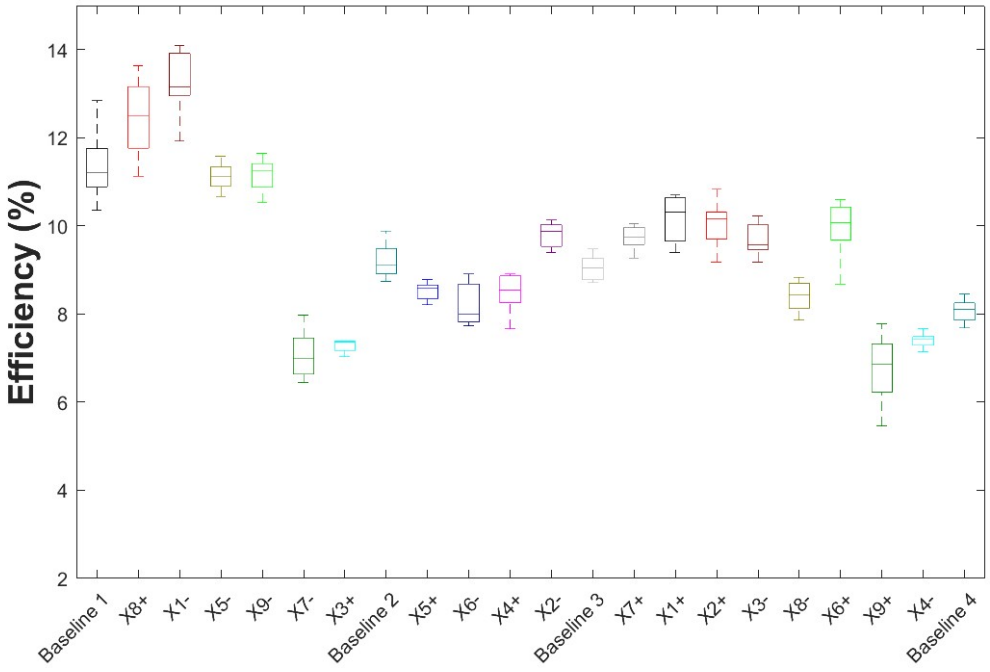

Figure 3.4: Boxplots of the efficiency of the OFAT experiment

Despite the fact that the baseline is not stable, the JMP software can still deduce several things from this experiment. In Figure 3.5 the software shows that there is a connection between the FF and the parameters X8 and X9. That is, the longer the post-anneal time T_3 shown in Figure 3.3 (X8) and the lower the pump out temperature (X9), the better the FF will be. Although it is important to remember that the accuracy of this model ($R_{sq} = 0.3$)[1] is mediocre due to baseline variations.

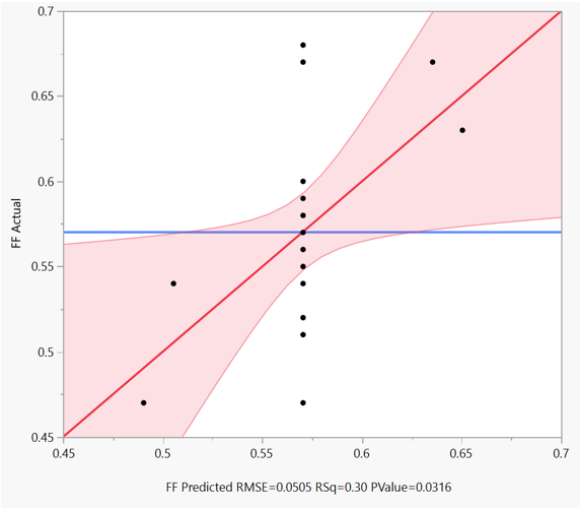

(a) Model fit for FF

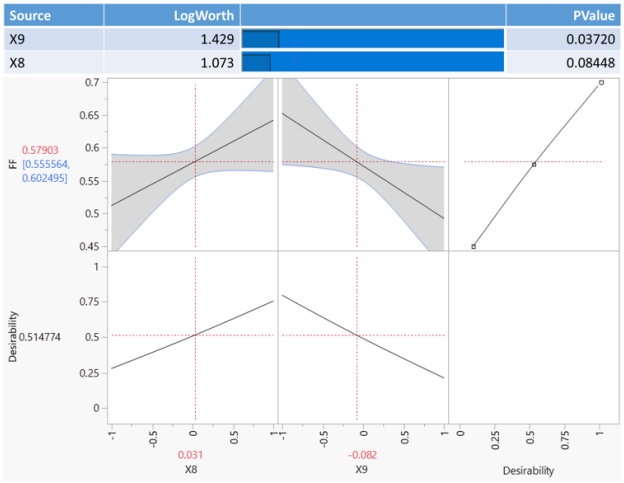

(b) model accuracy for FF

Figure 3.5: Influence of Post anneal time (X8) and pump out temperature (X9) on the FF

In Figure 3.6, a further observed correlation indicates that a decrease in ramp speed (X3) and an increase in annealing temperature (X4) have a positive effect on the V_{oc}. Furthermore, a longer total anneal time (X6 and X8) and again a lower pump-out temperature could be beneficial for the V_{oc}. All the other parameters (X1, X2, X5 and X7) seem to be less influential for a good absorber layer.

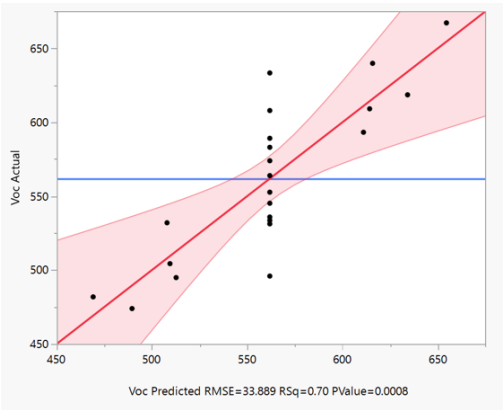

(a) Model fit for V_{oc}

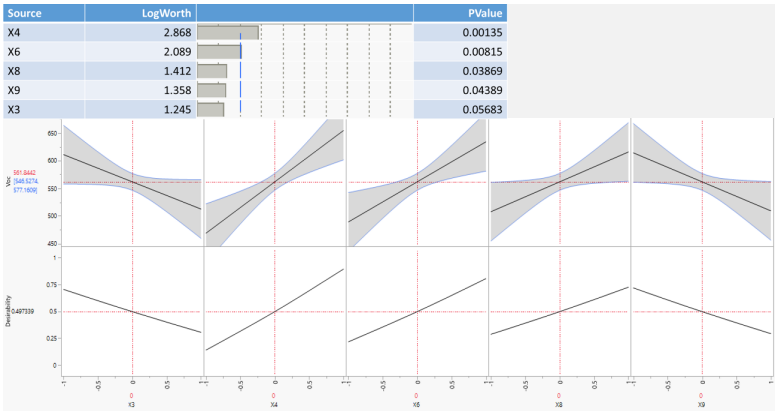

(b) model accuracy for V_{oc}

Figure 3.6: Influence of Ramping speed (X3), anneal temperature (X4), anneal time (X6), sulphurisation time (X8) and pump out temperature (X9) on the V_{oc}

[1] R_{sq} is known as the coefficient of determination. R_{sq} quantifies the strength of the linear relationship between the dependent variable and the independent variable. In the context of simple linear regression, R_{sq} is the square of the correlation coefficient, r. This metric, which ranges from 0 to 1, indicates the proportion of the total variance that is accounted for by the model. The closer R_{sq} is to 1, the greater the amount of variation that is explained by the model [23].

3.2 Baseline stability experiment

The first thing that needed to be solved after the OFAT experiment were the issues with the stability of the baseline. The sample is placed in a graphite box, and this graphite consumes and releases gasses to which it is exposed. After the OFAT experiment, the theory emerged that due to the excess amount of graphite, the box was not saturated and therefore consumed and released different amounts of gasses. To test the theory of this memory effect, a smaller box was designed (see Figure 3.7). For the design, the free software sketchUp (see Figures in Appendix B) was used and afterwards manufactured by an external company.

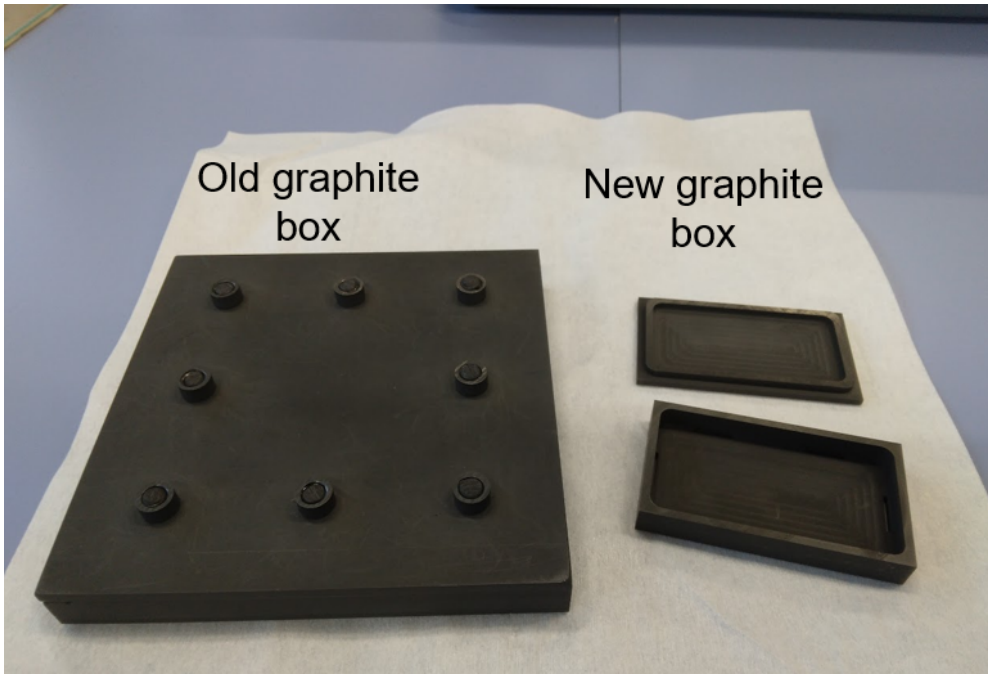

Figure 3.7: Old versus new graphite box

Another possible solution for this memory defect is to do a Zink oxide (ZnO) deposition on the inside of the graphite box (see Figure 3.8). This ZnO deposition will restrict the flow of gasses through the graphite because it is more dense than the porous graphite. With these two boxes, the baseline recipe of the OFAT experiment was run multiple times.

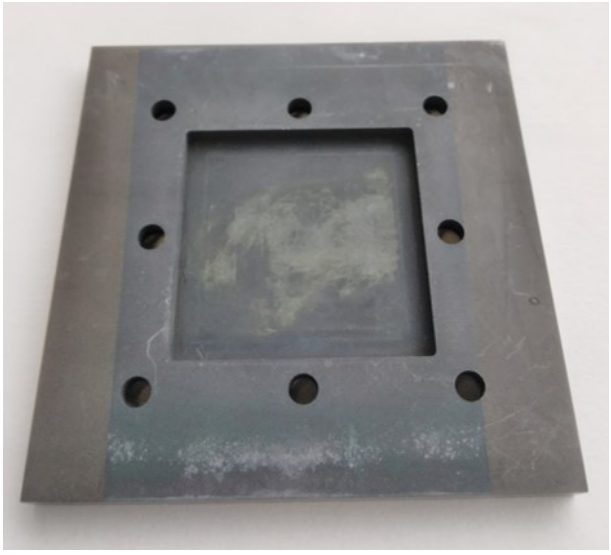

Figure 3.8: Graphite box after ZnO depositioning

3.2.1 Results and discussion

In this subsection, the efficiency results of the newly designed graphite box and the old box with the ZnO layer are discussed. The results can be found in Figure 3.9.

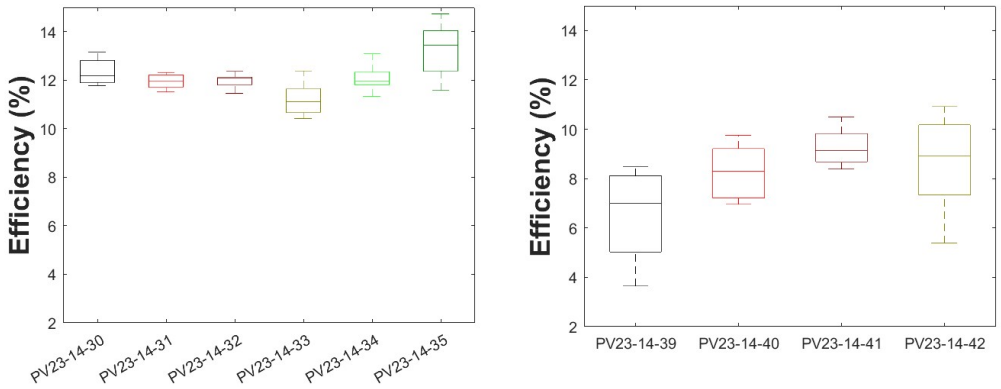

(a) New designed small box (b) Old box with ZnO layer

Figure 3.9: Efficiency comparison between new box and old ZnO deposited box

The newly designed small box demonstrates robust and stable results with consistent performance, achieving an average efficiency of 12%.The last sample PV-23-14-35 even had an average efficiency of 13.3%, but this is because the grid size was changed from 4mm by 4mm to 2.5mm by 2.5mm. The reason for changing this grid size was that the larger the cell, the greater the distance to the probes of the oriel IV-setup and this resulted in energy losses. Normally, the use of grid fingers is advised, because then the horizontal distance that has to be covered is smaller. However, these grid fingers were not available during the period of this master's thesis and therefore the choice was made to use the 2.5mm by 2.5mm grid. On the other hand, the samples run in the old box with the ZnO layer all had a grid size of 4mm by 4mm and are less stable and also have a lower average efficiency of 8%. Consequently, the decision was made to discontinue the ZnO deposition technique in favor of adopting the newly designed smaller box and using samples with a grid size of 2.5mm by 2.5mm in future experiments.

3.3 Finding a new baseline

Following resolution of the stability issue and the establishment of consistent baselines, it is now feasible to apply the insights obtained from the OFAT experiment. In Table 3.2 the important parameters of the old baseline recipe can be found together with the beneficial results of the OFAT experiment. Because time limitations did not allow us to proceed to a Full Factorial Design (FFD) experiment, we still tried to improve the baseline efficiency based on the OFAT experiment, by varying the parameters in the direction indicated by the results of the OFAT experiment untill a favorable result is reached.

Table 3.2: Conclusions of important parameters from OFAT versus the old baseline

Parameters	Unit	Old baseline	OFAT
Ramping speed	C/s	10	2
Anneal Temperature	C	570	590
Anneal Time T_1 + T_2	min	5+5	10+10
Post-anneal Time T_3	min	1	3
Pump out temperature	C	400	100

3.3.1 Results and discussion

In this subsection, the results of the new baseline search are discussed. The new baseline parameters can be found in Table 3.3 and Figure 3.10 compares the results of the new and the old baseline. In the first run (PV23-14-36), all important parameters were changed to the suggested parameters of the OFAT experiment (shown in Table 3.2). The average efficiency of this run was 12.8%. However, of greater significance was the observation that, at the core of the sample, the absorber layer delaminated. The assessment was made that the long duration and high temperatures were a possible cause of the delaminiation. Therefore, the next runs are executed with lower anneal temperatures and less long anneal time ($T_1 + T_2$), resulting in a new baseline recipe shown in Table 3.3. Although delamination still occurs, this is much less than in the previous samples.

Table 3.3: new baseline versus old baseline

Parameter number	Parameters	Unit	Old baseline	New Baseline
X1	H_2S pressure T_0	mbar	30	30
X2	N_2 pressure T_0	mbar	670	670
X3	Ramping speed	C/s	10	2
X4	Anneal temperature	C	570	550
X5	H_2S flow during T_1	sccm	20	20
X6	Anneal time T_1 + T_2	min	5+5	5+5
X7	H_2S pressure post-anneal	mbar	20	20
X8	Post-anneal yime T_3	min	1	3
X9	Pump out temperature	C	400	100

In Figure 3.10 a comparison has been made between the old baseline (PV23-14-35) and the new baseline (PV23-14-38). The baseline efficiency (3.10a) increased from an average efficiency of 13.3% to 15.2% with a champion cell of 15.9%. The V_{oc} (3.10c) and the FF (3.10b) increase, only the J_{sc} (3.10d) stays more or less the same. Examining the resistances, an enhancement can also be seen, with the R_s (3.10e) diminishing and the R_{sh} (3.10f) increasing with the new baseline. It is desirable for R_s to be minimized since it represents the total resistance of the cell. A greater value of R_{sh} is generally favored. Because reduced R_{sh} leads to power losses in solar cells by offering a secondary pathway for the current produced by light [6].

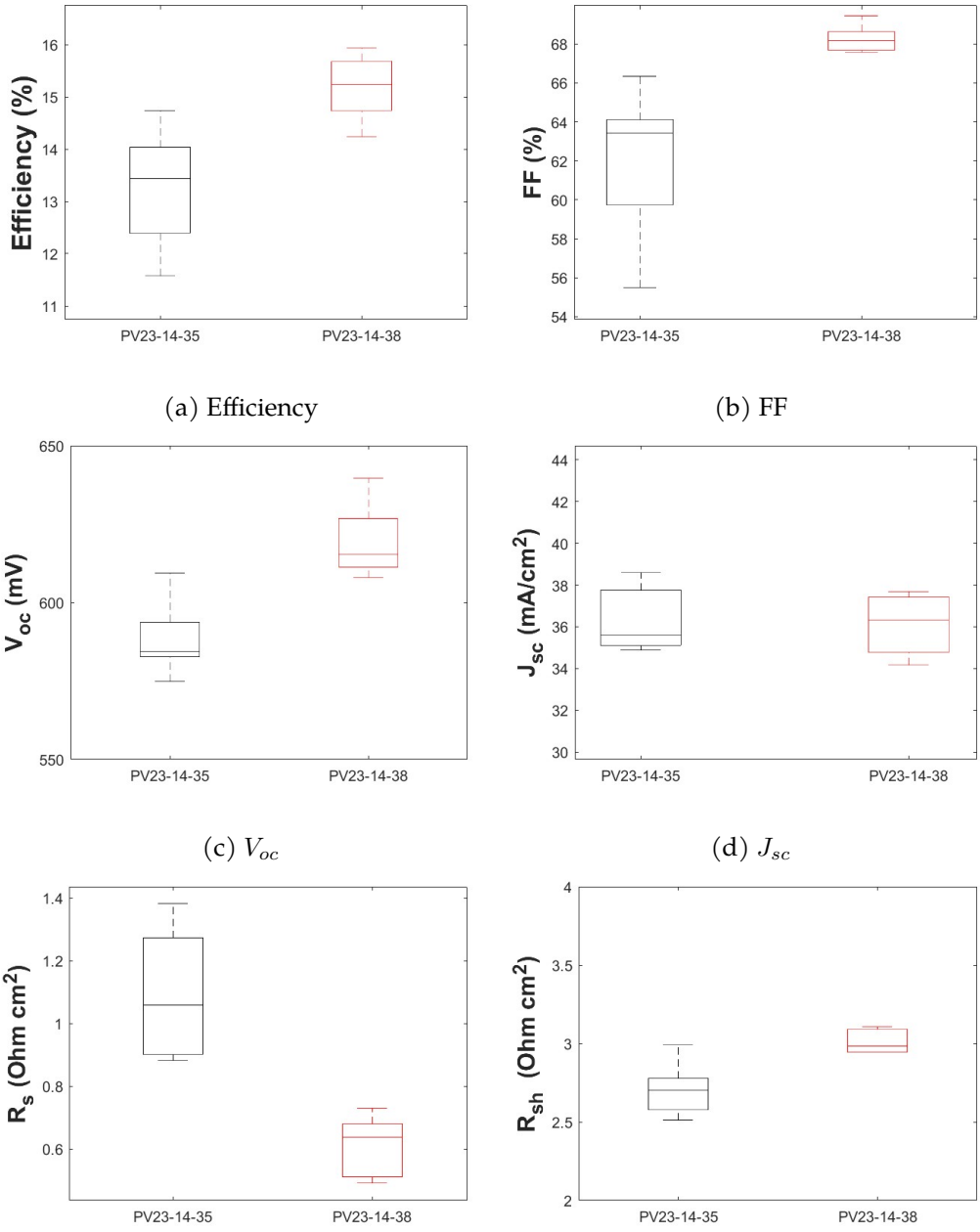

(a) Efficiency

(b) FF

(c) V_{oc}

(d) J_{sc}

(e) R_s

(f) R_{sh}

Figure 3.10: comparing the old with the new baseline

3.4 Anti reflection coating

To improve the efficiency of our champion cells of sample PV23-14-38 a anti-reflective coating (ARC) of magnesium fluoride (MgF_2) was applied on top of the ITO. There are two main reasons for applying the MgF_2 treatment, namely:

1. **To minimize reflextion at the interface between the air and the solar cell surface** because MgF_2 has a refractive index of about 1.38, which is intermediate between that of air (≈ 1) and the CIGS absorber layer ($\approx 2.4 - 2.9$). This refractive index creates a gradient that significantly reduces reflection through destructive interference.
2. MgF_2 is **highly transparent over a wide range of wavelengths**, particularly in the visible and near-infrared spectrum (300 nm to 1200 nm). This transparency ensures that most of the incident light passes through the coating and reaches the CIGS absorber layer.

3.4.1 Results and discussion

In this subsection, the champion cells (before and after MgF_2) are compared with the champion cells of the world record (shown in Table 3.4). This will show the areas where our cells can still improve and what values we need to strive for.

Table 3.4: Comparison of the champion cell versus the world record [24, p.469]

Sample	V_{oc} **(mV)**	J_{sc}**(mA/cm²)**	**FF (%)**	η **(%)**	E_g **(eV)**	**ARC**	**Ag**	**PDT**
PV23-14-38	615	37.7	68	15.93	1.10	-	No	-
PV23-14-38 +ARC	625	39.8	67.3	16.76	-	MgF_2	No	-
World record	767	38.3	80.5	23.64	1.13	MgF_2	Yes	RbF

Table 3.4 shows that the ARC of sample PV23-14-38 results in a slightly higher V_{oc}, J_{sc} and although the FF drops a little, the efficiency of the champion cell increases from 15.9% to 16.7%.

When discussing the results between the world record and sample PV23-14-38 after ARC, it is important to know what choices were made during the production process of these cells. First and foremost, the world record cells were made using multistage co-evaporation (see section 2.2.1.1). This made it possible to evaporate more Ga close to the Mo back contact and a lower steady concentration towards the CdS buffer layer. This distribution helps minimizing both lateral and depth-related bandgap fluctuations, thereby reducing losses in open-circuit voltage [24]. And this is not possible with our sample because it is made with the two-step process and during selenizatiton this kind of control is not possible. The second difference was that in the absorber layer of the world record cells Silver was added in a ratio of $\frac{Ag}{Ag+Cu} = 0.19$. And the third and final difference was that for the world record a Post-deposition treatment of Rubidium fluoride was used and for our samples no PDT was done [24]. There are four reasons for applying a PDT treatment, namely:

1. **Passivation of grain boundaries** because grain boundaries can act as recombination centers for charge carriers (electrons and holes), hereby reducing the efficiency of the solar cell. The RbF treatment helps to passivate these grain boundaries, reducing recombination losses and improving the overall efficiency of the solar cell.
2. The RbF treatment will **reduce the density of interface states between the CdS and absorber layer** by filling in the defects and therefore reducing the the recombination losses.
3. RbF helps to **reduce reflection losses** at the front surface of the solar cell, thereby increasing light absorption.
4. **Stability enhancement** due to the extra coating of RbF thereby protecting it against oxygen or moisture.

If we look at the numbers we see that the V_{oc} and FF of the world record are better, but our sample has the best J_{sc}. If we take a look at the bandgap energy (E_g) we see that they are both close to the ideal value of 1.15 eV found in literature [24]. To further improve our CIGS solar cells the addition of a PDT and Ag could be useful.

In this concluding chapter, we summarize the key findings of this Master's thesis and provide an outlook on future research directions in the field of thin film chacogenide solar cells.

This study was designed to investigate the baseline process of Copper indium gallium disulfide diselenide $Cu(In,Ga)(S,Se)_2$ (CIGS) absorber layers produced with the two-step method. Through a combination of an One Factor A Time and baseline stability experiments, we have made several significant findings:

1. **The graphite box was the issue of the baseline stability:** because during the selenization process the graphite is exposed to H_2S gasses and some of these gasses are absorbed by the graphite box. Because the graphite box was not saturated, it therefore consumed and released different amounts of gasses during different experiments.
2. **Ramping speed, anneal temperature, total annealing time** $(T_1 + T_2 + T_3)$ **and pump out temperature are the most important parameters** that must be changed in our selenization process recipe. All other parameters seem to be less influential.
3. **High temperatures and long anneal times can enhance the delamination** of the absorber layer. Because when the anneal temperature and anneal time were reduced, a reduction of the delamination occurred.

All of this led us to successfully increase the efficiency of our champion cells from 13.3% to 16.7%. Although this thesis has addressed several important questions, there are still many avenues for further exploration and research in this area. Some potential directions for future studies include:

1. **the setup of an Full Factorial Design (FFD) experiment** were the relation between the most important parameters is investigated. In Table 4.1 a suggestion of parameters and parameter values was made as to how I would approach it.
2. **More research can be done on addition of a Post-deposition treatment (PDT)** such as RbF and CsF to the process.
3. **Adding Silver in the metal precursor**.

Table 4.1: FFD parameters

Parameter number	Parameters	Unit	-	0	+
X1	Ramping speed	C/s	0,3	2	3
X2	Anneal temperature	C	540	550	560
X3	Anneal time T_1 + T_2	min	3+3	5+5	7+7
X4	Post-anneal time T_3	min	1	3	6

In addition to these specific research directions, ongoing advancements in Copper indium gallium disulfide diselenide $Cu(In,Ga)(S,Se)_2$ research offer exciting opportunities for further innovation and discovery.

As we move forward, it is essential to continue building upon the findings of this thesis, collaborating with colleagues, and exploring new avenues for research. By doing so, we can contribute to

the advancement of knowledge in thin film chalcogenide solar cell baselines and make meaningful contributions to solar cell industry.

[1] Billel Salhi. "The Photovoltaic Cell Based on CIGS: Principles and Technologies". In: *Materials* 15.5 (Mar. 2022), pp. 1–27. ISSN: 19961944. DOI: 10.3390/ma15051908.

[2] Antonio Luque and Steven Hegedus, eds. *Handbook of photovoltaic science and engineering*. Vol. 13. New Jersey: John Wiley and Sons Ltd, Apr. 2003, pp. 567–616. ISBN: 0471491969. DOI: 10.1002/0470014008.

[3] A. Urbaniak et al. "Consequences of grain boundary barriers on electrical characteristics of CIGS solar cells". In: *Solar Energy Materials and Solar Cells* 253 (Feb. 2023), pp. 1–9. ISSN: 09270248. DOI: 10.1016/j.solmat.2023.112252. URL: https://doi.org/10.1016/j.solmat.2023.112252.

[4] Annealsys. *Annealsys AS-one furnace*. URL: https://www.annealsys.com/products/rtp-and-rtcvd/as-one.html.

[5] a.s. Tescan group. *SEM EDS Tescan*. URL: https://www.tescan.com/product/sem-for-materials-science-tescan-vega/.

[6] Stijn Driessen. *Development of ultra-thin CIGS absorber material with alkali treatment for solar cell production* [*Masterthesis*]. Diepenbeek: Uhasselt, 2021, pp. 1–40. URL: http://hdl.handle.net/1942/35045.

[7] Udai P Singh and Nandu B Chaure. *Recent Advances in Thin Film Photovoltaics*. Springer Singapore, Sept. 2022. ISBN: 978-981-19-3723-1. DOI: https://doi.org/10.1007/978-981-19-3724-8.

[8] Sreekanth Mandati et al. "Copper Chalcopyrites for Solar Energy Applications". In: *Transactions of the Indian Institute of Metals* 72.2 (Feb. 2019), pp. 271–288. ISSN: 09751645. DOI: 10.1007/s12666-018-1455-0.

[9] Shigeru Niki et al. "CIGS absorbers and processes". In: *Progress in Photovoltaics: Research and Applications* 18.6 (Sept. 2010), pp. 453–466. ISSN: 10627995. DOI: 10.1002/pip.969.

[10] Jeyakumar Ramanujam and Udai P. Singh. "Copper indium gallium selenide based solar cells - A review". In: *Energy and Environmental Science* 10.6 (June 2017), pp. 1306–1319. ISSN: 17545706. DOI: 10.1039/c7ee00826k. URL: https://www.researchgate.net/publication/316284337.

[11] A. Romeo et al. "Development of thin-film Cu(In,Ga)Se2 and CdTe solar cells". In: *Progress in Photovoltaics: Research and Applications* 12.2-3 (2004), pp. 93–111. ISSN: 10627995. DOI: 10.1002/pip.527.

[12] Yi Ren. *CZTSSe film formation by selenization/sulfurization of metal coatings* [*Master thesis*]. 2011.

[13] T. Klinkert et al. "Ga gradients in Cu(In,Ga)Se2: Formation, characterization, and consequences". In: *Journal of Renewable and Sustainable Energy* 6.1 (Aug. 2014), pp. 1–11. ISSN: 19417012. DOI: 10.1063/1.4866255. URL: http://dx.doi.org/10.1063/1.4866255.

[14] C. A. Kaufmann et al. "Depth profiling of Cu(In,Ga)Se2 thin films grown at low temperatures". In: *Solar Energy Materials and Solar Cells* 93.6-7 (Oct. 2009), pp. 859–863. ISSN: 09270248. DOI: 10.1016/j.solmat.2008.10.009.

[15] M Sc Penghui Yang. "Impact of Alkali Treatments on the Surface and Interface Properties of Chalcopyrite Thin-Film Solar Cell Absorbers". PhD thesis. Cottbus–Senftenberg: Universität Cottbus–Senftenberg, May 2020, pp. 1–147.

[16] Chris Eberspacher, Karen Pauls, and Jadc Serra. "Non-vacuum processing of CIGS solar cells". In: New Orleans, LA, USA: IEEE, Apr. 2003, pp. 684–687. ISBN: 0-7803-7471-1. DOI: 10.1109/PVSC.2002.1190657.

[17] Vijay K. Kapur et al. "Non-vacuum processing of CuIn1-xGaxSe2 solar cells on rigid and flexible substrates using nanoparticle precursor inks". In: *Thin Solid Films* 431-432 (May 2003), pp. 53–57. ISSN: 00406090. DOI: 10.1016/S0040-6090(03)00253-0.

[18] Alice Debot et al. "Inkjet-printed indium sulfide buffer layer for Cu(In,Ga)(S,Se)2 thin film solar cells". In: *Thin Solid Films* 745 (Mar. 2022). ISSN: 00406090. DOI: 10.1016/j.tsf.2022.139096.

[19] Seong Yeon Kim and Jun Ho Kim. "Fabrication of CIGS thin films by using spray pyrolysis and post-selenization". In: *Journal of the Korean Physical Society* 60.12 (June 2012), pp. 2018–2024. ISSN: 03744884. DOI: 10.3938/jkps.60.2018.

[20] Qijie Guo et al. "Sulfide nanocrystal inks for dense Cu(In 1-xGa x)(S 1-ySe y) 2 absorber films and their photovoltaic performance". In: *Nano Letters* 9.8 (June 2009), pp. 3060–3065. ISSN: 15306984. DOI: 10.1021/nl901538w.

[21] Chia Hua Huang et al. "Deposition technologies of high-efficiency cigs solar cells: Development of two-step and co-evaporation processes". In: *Crystals* 8.7 (July 2018), pp. 1–17. ISSN: 20734352. DOI: 10.3390/cryst8070296.

[22] Sarallah Hamtaei et al. "Dominant processing factors in two-step fabrication of pure sulfide CIGS absorbers". In: *Energies* 14.16 (Aug. 2021). ISSN: 19961073. DOI: 10.3390/en14164737. URL: https://doi.org/10.3390/en14164737.

[23] *JMP Statistical Knowledge Portal* [*Online*]. URL: https://www.jmp.com/en_my/statistics-knowledge-portal/what-is-regression/interpreting-regression-results.html.

[24] Jan Keller et al. "High-concentration silver alloying and steep back-contact gallium grading enabling copper indium gallium selenide solar cell with 23.6% efficiency". In: *Nature Energy* 9 (Apr. 2024), pp. 467–478. ISSN: 20587546. DOI: 10.1038/s41560-024-01472-3. URL: https://www.nature.com/articles/s41560-024-01472-3.

[25] David B. Mitzi. "Solution processing of chalcogenide semiconductors via dimensional reduction". In: *Advanced Materials* 21.31 (Aug. 2009), pp. 3141–3158. ISSN: 09359648. DOI: 10.1002/adma.200802027. URL: https://doi.org/10.1002/adma.200802027.

[26] Dong Yeup Lee, Sejun Park, and Junho Kim. "Structural analysis of CIGS film prepared by chemical spray deposition". In: *Current Applied Physics* 11 (Jan. 2011), pp. 88–92. ISSN: 15671739. DOI: 10.1016/j.cap.2010.11.089.

[27] National Renewable Energy Laboratory. *Chart of highest confirmed conversion efficiencies for research cells for a range of photvoltaic technologies, plotted from 1976 to present*. URL: https://www.nrel.gov/pv/cell-efficiency.html.

A APPENDIX

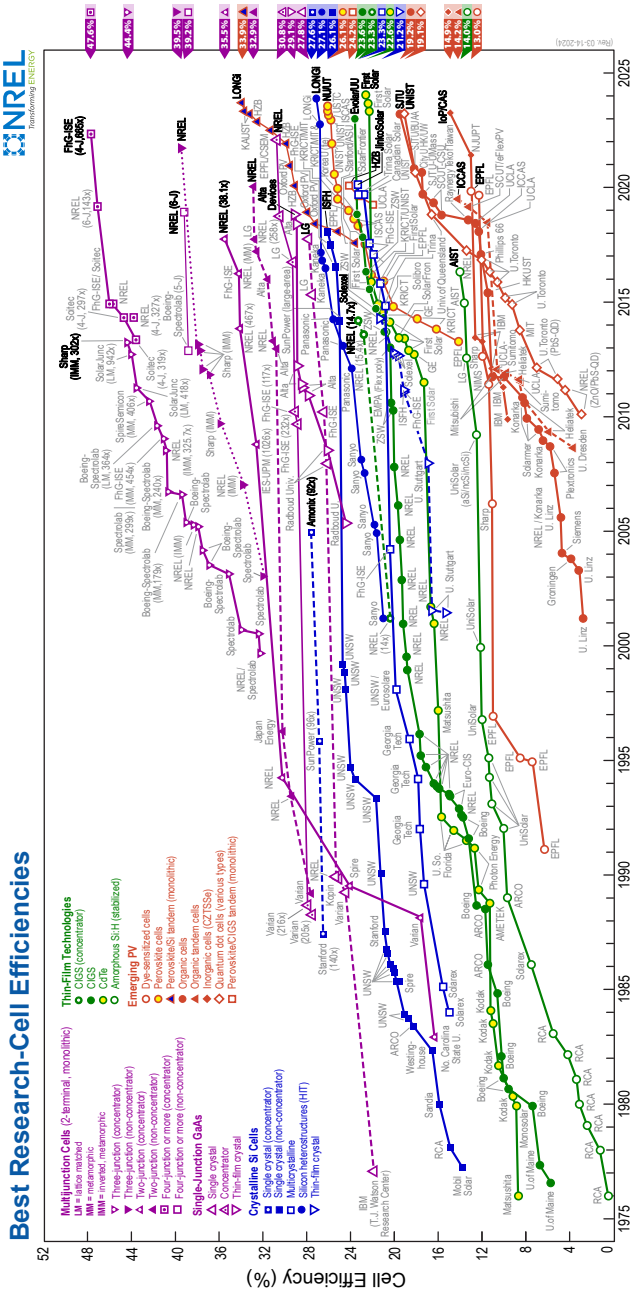

Figure A.1: Best solar cell efficiencies[27]
This plot is courtesy of the National Renewable Energy Laboratory, Golden, CO

B APPENDIX

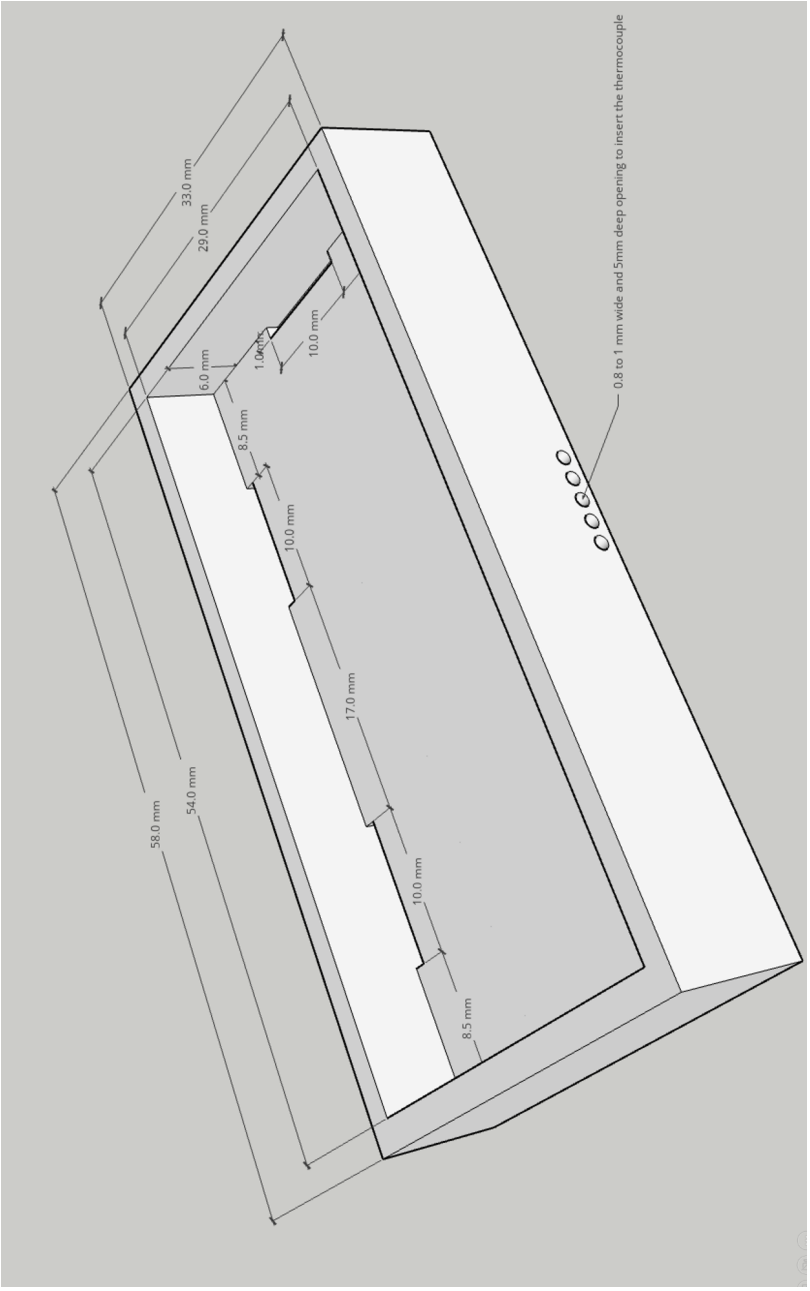

Figure B.1: small graphite box 3D design

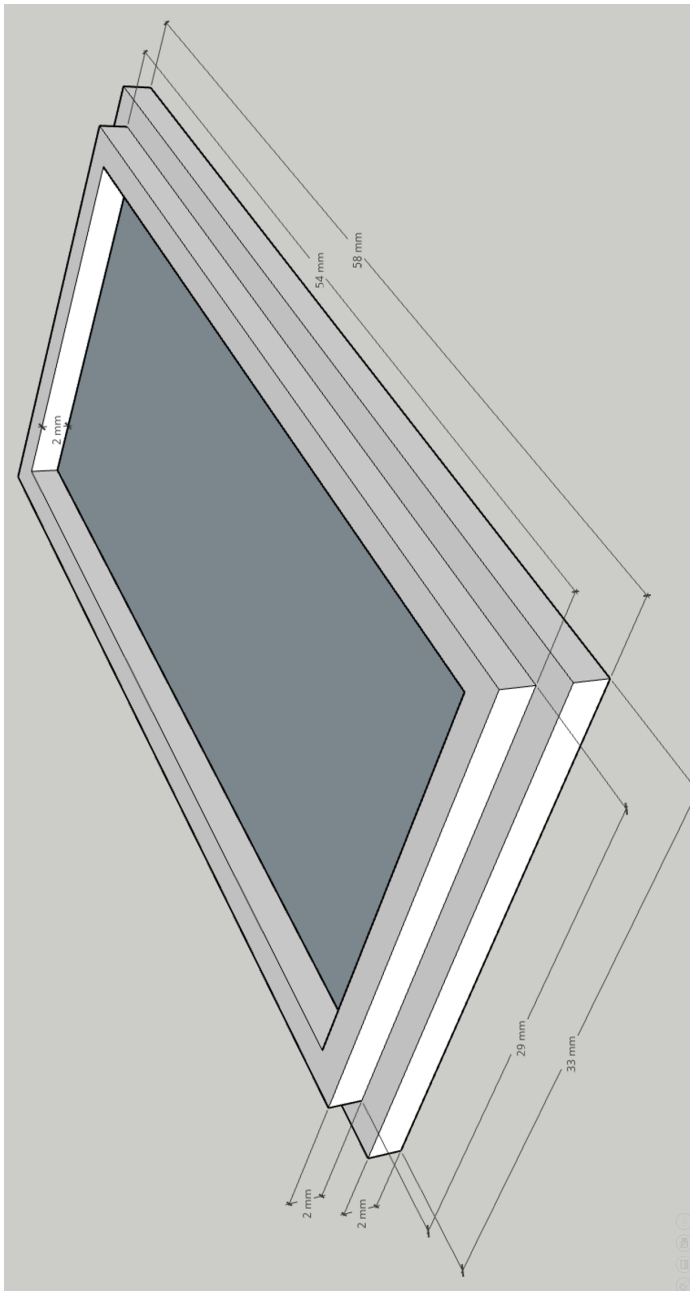

Figure B.2: lid for small graphite box 3D design